THE ASTROPHYSICAL JOURNAL, 429:268–284, 1994 July 1

THE VELOCITY STRUCTURE OF THE COMETARY H II REGIONS G13.87+0.28, G32.80+0.19B, AND G61.48+0.09B1

GUIDO GARAY
Departamento de Astronomía, Universidad de Chile, Casilla 36-D, Santiago, Chile
SUSANA LIZANO
Instituto de Astronomía, Universidad Nacional Autónoma de México, Apdo. Postal 70-264, 04510 México, D.F., Mexico
AND
YOLANDA GÓMEZ[1]
Very Large Array, National Radio Astronomy Observatory, P.O. Box 0, Socorro, NM 87801
Received 1993 July 29; accepted 1993 December 9

ABSTRACT

We present H92α radio recombination line and radio continuum observations toward three cometary-like H II regions, G13.87+0.28, G32.80+0.19B, and G61.48+0.09B1, with an angular resolution of ~2″. The kinematics (H92α velocity and line-width fields) and morphology (continuum maps) of the ionized gas from two of these sources, G32.80+0.19B and G61.48+0.09B1, are best explained by models in which the ionized gas is expanding in an anisotropic medium (champagne models), whereas that of G13.87+0.28 can be well explained in terms of a bow shock formed by the stellar wind of a massive star moving supersonically through a molecular cloud.

As predicted theoretically, we find that at the frequency of the H92α line non-LTE effects are significant, particularly for the compact, high emission measure H II regions we detected in the direction of two cometary regions.

Subject headings: H II regions — ISM: individual (G13.87+0.28, G32.80+0.19, G61.48+0.09) — radio lines: ISM

1. INTRODUCTION

The morphology of compact regions of ionized gas provides valuable information for understanding the dynamical interaction between the gas excited by a newly formed star and the neutral surrounding medium. Accordingly, and because of the recent advent of instruments providing high angular resolution, the structure of compact H II regions has been the subject of intense current studies (Wood & Churchwell 1989; Fey et al. 1992; Garay et al. 1993; Kurtz, Churchwell, & Wood 1994). A remarkable result from these studies is that a significant number (about 20%) of the compact H II regions have cometary morphologies. This type of H II region, the prototype of which is the source G34.26+0.15 (Reid & Ho 1985; Garay, Rodríguez, & van Gorkom 1986), is characterized by having a bright compact head and a diffuse, low-brightness, extended tail.

Two main types of physical models have been proposed to explain cometary H II regions: champagne flows and stellar wind bow shocks. In the former (Tenorio-Tagle 1979; Bodenheimer, Tenorio-Tagle, & Yorke 1979) the cometary region is understood in terms of an ionized gas expanding in a medium with strong density gradients. In the latter (Van Buren et al. 1990; Mac Low et al. 1991) the cometary morphology is explained as a bow shock supported by the stellar wind of an ionizing star that is moving supersonically through the ambient molecular cloud. The determination of the actual origin of cometary H II regions is certainly an important task, since it would contribute to our understanding of the role of stellar winds in the early stages of evolution of massive stars and/or about the characteristics of the medium in which these stars are formed.

Theoretical radio continuum maps of H II regions in the champagne phase, namely, the phase in which the ionization front of an H II region crosses a region with strong density gradients, such as the boundary of a molecular cloud, have been presented by Yorke, Tenorio-Tagle, & Bodenheimer (1983). Maps of compact H II regions modeled as bow shocks have been presented by Mac Low et al. (1991). Both calculations reproduce well the observed radio morphology of cometary H II regions. Thus, based purely on morphological information it is difficult to discern whether it is the champagne or the wind model that best explains cometary H II regions.

There are, however, notable differences in other predictions of these models, particularly regarding the kinematical properties of the ionized gas. The champagne flow models predict that the velocity of the ionized gas near the coma should be similar to the molecular gas velocity, while near the tail it should reach velocities of about 2–3 times the sound speed in the H II region. The bow shock model, on the other hand, predicts that the ionized gas in the coma should be moving with respect to the molecular gas. The gas near the head should be stationary with respect to the star, while the gas along the trailing edge should be nearly at rest with respect to the molecular cloud. Regarding velocity gradients, the bow shock model predicts that they should be steeper in front of the arc than behind it, while the champagne flow model predicts that they are largest in the tail, where the gas is accelerated out the nozzle.

Thus, a possible way to discriminate among the champagne flow and bow shock models would be through the determi-

[1] On leave from Instituto de Astronomía, Universidad Nacional Autónoma de México.

TABLE 1

INSTRUMENTAL PARAMETERS

SOURCE	PHASE-TRACKING CENTER α(1950)	PHASE-TRACKING CENTER δ(1950)	SYNTHESIZED BEAM	rms NOISE[a] (mJy beam^{-1})
G13.87+0.28.....	$18^h11^m41^s.7$	−16°46′37″.0	2″.9 × 1″.9	0.32
G32.80+0.19.....	18 47 57.0	−0 05 34.0	2.3 × 2.2	0.32
G61.48+0.09.....	19 44 42.6	25 05 21.2	2.4 × 2.1	0.25

[a] 1 σ rms noise in a line channel.

nation of the velocity field of the ionized gas. Because compact H II regions are embedded in dense molecular clouds, in which they were formed or through which they are moving, they are invisible at ultraviolet and optical wavelengths. On the other hand, radio emission escapes from the clouds unaffected by the dust, hence radio observations offer a unique way to investigate the physical conditions of the gas around recently formed stars. In particular, radio recombination lines constitute an excellent probe to determine the velocity structure of the gas in compact H II regions. In this paper we present radio recombination line observations toward three compact H II regions classified as of cometary shape by Garay et al. (1993). Our main goal was to obtain the velocity structure of the gas across these regions, which would help to establish the origin of the cometary morphology.

2. OBSERVATIONS

The observations were made with the Very Large Array of the National Radio Astronomy Observatory[2] in the spectral line system on 1992 April 20. The array was in the C configuration, which provides a shortest spacing of 73 m and a longest spacing of 3.4 km. This range of spacings makes structures larger than about 60″ undetectable at 3.6 cm.

We observed the H92α recombination line, at the rest frequency of 8309.383 MHz, toward three regions of ionized gas: G13.87+0.28, G32.80+0.19, and G61.48+0.09. We used a bandpass of 6.25 MHz, centered at an LSR velocity of 28 km s^{-1}, and 31 spectral channels each 195.3 kHz wide (7.05 km s^{-1} at the frequency of the H92α line). The integration times on source were ∼130 minutes for G13.87+0.28 and G61.48+0.09, and ∼100 minutes for G32.80±0.19. Each 15 minute scan on source was preceded and followed by a 4 minute phase calibration scan. The data were edited and calibrated by applying the complex gain solution from the calibration sources. The flux density scale was determined by observing 3C 286, for which we assumed a flux density of 5.33 Jy at 3.6 cm. The bandpass response was normalized using the observations of the bandpass calibrators 1226±023 and 0316±413.

The spectral data were further calibrated by applying the solution obtained from a self-calibration on the continuum channel, which contains the average of the central 75% of the bandpass. The (*u*, *v*) data were Fourier-transformed and cleaned using the MX algorithm. The synthesized beams and the rms noise level in a single spectral line channel map are given in Table 1.

[2] The National Radio Astronomy Observatory is operated by Associated Universities, Inc., under cooperative agreement with the National Science Foundation.

3. RESULTS

3.1. *Radio Continuum*

The self-calibrated maps of the observed sources, made using the continuum channel containing 75% of the total bandwidth of 6.25 MHz, are shown in Figure 1. The observed parameters of the individual H II regions derived from the radio continuum observations are summarized in Table 2.

3.1.1. *G13.87+0.28*

Our map, made with an angular resolution of 2″.9 × 1″.9 at P.A. −19°, shows that this source has a bright compact head, with a sharp edge toward the southwest, and a long tail trailing to the northeast. This radio continuum structure is in good agreement with that observed at 4.9 GHz by Garay et al. (1993). The morphology of G13.87+0.28 is roughly symmetric about a line at P.A. ∼15°, passing through $\alpha = 18^h11^m41^s.83$, $\delta = -16°46'38''.3$, which we will refer to hereafter as its symmetry axis. At 8.3 GHz we measured a total flux density of 3.2 Jy and a peak brightness temperature of 192 K, implying that this region is optically thin at this frequency.

3.1.2. *G32.80+0.19*

The 8.3 GHz continuum image, made with an angular resolution of 2″.3 × 2″.2 at P.A. −25°, shows that this source has a complex structure, which we model as a bright, compact component (labeled A), an extended cometary-like component toward the northeast (labeled B), and a weak unresolved source toward the northwest (labeled C). Our map is in good agreement with the 4.9 GHz image presented by Garay et al. (1993). We measured peak brightness temperatures at 8.3 GHz of 2700, 1200, and 55 K for components A, B, and C, respectively. In the higher angular resolution observation at 2 cm by Kurtz et al. (1994), the emission from component A is resolved into two distinct components, while emission from component B is detected only from the head structure, the tail being completely resolved out. The 8.3 GHz flux density integrated over the whole region is 3.8 Jy, similar to the value of 3.6 Jy at 8.1 GHz measured by Wink, Altenhoff, & Mezger (1982).

3.1.3. *G61.48+0.09*

The G61.48+0.09 region was previously interferometrically mapped at 5 GHz by Felli & Harten (1981) and at 1.5 and 5 GHz by Garay et al. (1993). These radio maps show that G61.48+0.09 is composed of two distinct features, referred as S88B1 and S88B2. Our 8.3 GHz map, made with an angular resolution of 2″.4 × 2″.1 at P.A. −24°, clearly resolves both components into an extended cometary-like H II region toward the west (S88B1) and a compact region toward the east (S88B2), in good agreement with the 4.9 GHz image of Garay et al. (1993). We measured peak brightness temperatures at 8.3 GHz of 380 and 550 K for components B1 and B2, respec-

TABLE 2

OBSERVED PARAMETERS OF THE H II REGIONS

SOurce	α(1950)[a]	δ(1950)[a]	Peak Flux (Jy beam^{-1})	Flux Density (Jy)	Deconvolution Size
G13.87+0.28	18^{h}11^{m}41^s.92	−16°46′35″.3	0.044	3.2	20″
G32.80+0.19A	18 47 56.82	−0 05 33.7	0.76	1.4	2.0
G32.80+0.19B	18 47 57.07	−0 05 28.9	0.26	2.2	6.1
G61.48+0.09B1	19 44 42.53	25 05 21.2	0.089	3.5	14
G61.48+0.09B2	19 44 43.43	25 05 20.3	0.154	0.7	3.5

[a] Peak position.

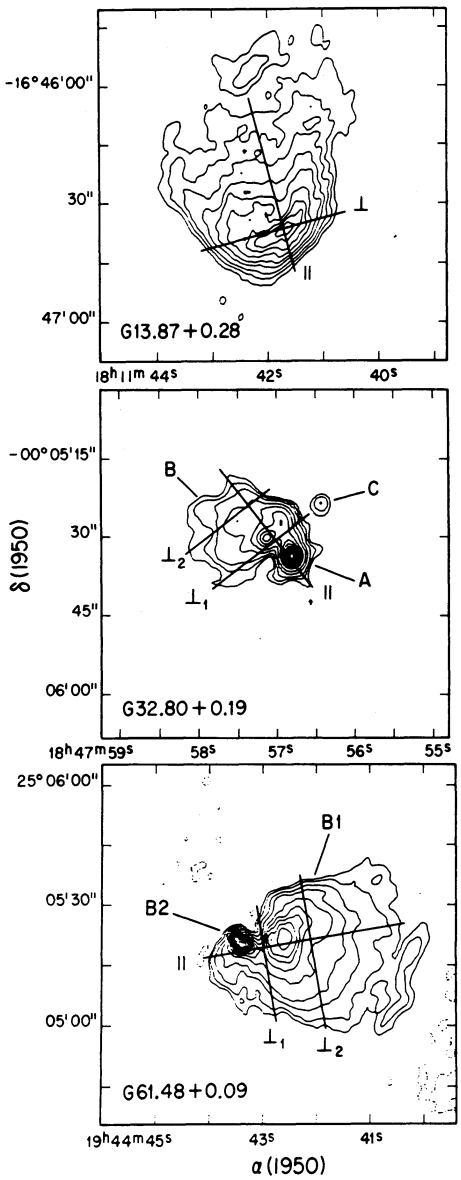

FIG. 1.—VLA continuum maps toward cometary-like H II regions at 8.3 GHz. *Top:* G13.87+0.28 region. Contour levels are −2, 2, 5, 10, 20, 30, 45, 60, 75, and 90% of the peak brightness of 59.7 mJy beam^{-1}. The angular resolution is 2″.9 × 1″.9. *Middle:* G32.80+0.19 region. Contour levels are −0.5, 0.5, 1, 2, 5, 10, 20, 30, 40, 50, 60, 70, 80, and 90% of the peak brightness of 0.795 Jy beam^{-1}. The angular resolution is 2″.3 × 2″.2. *Bottom:* G61.48+0.09 region. Contour levels are −1, 1, 2, 5, 10, 20, 30, 40, 50, 60, 70, 80, and 90% of the peak brightness of 0.154 Jy beam^{-1}. The angular resolution is 2″.4 × 2″.1. The lines drawn in the figures are the slices referred to in the text and following figures as parallel and perpendicular strips.

tively, suggesting that both regions are optically thin at this frequency.

3.2. H92α *Line*

To produce maps of line emission, we subtracted from each individual channel map a continuum map made from the average of off-line channels. The observed spectra of the H92α line emission integrated over the whole area of each individual H II region, and fitted Gaussian profiles, are shown in Figure 2. The fitted line parameters are summarized in Table 3.

Images of the line-center velocity and line width of the H92α line emission were obtained in two ways: (1) by computing moments of the line flux density, using the AIPS task MOMNT, and (2) from Gaussian fits to the spectrum at each pixel in the image which showed channels with a flux density 5 times greater than the 1 σ rms noise in the line channel maps. Both procedures gave similar values for the line-center velocity and line width. We note that the moment method gives the velocity dispersion, σ_v, which, to be converted to a FWHM line width, Δv, should be multiplied by 2.355. In what follows we present a detailed description of the spatial and velocity structure of the H92α emission from each object. The images of the integrated line flux density, line-center velocity, and line width shown hereafter correspond to those derived using the moment method.

3.2.1. *G13.87+0.28*

Individual line maps of the H92α emission from G13.87+0.28 are shown in Figure 3. Line emission was detected in the velocity range from 35.1 to 70.3 km s^{-1}.

Center velocities.—The central velocity of the H92α line emission integrated over the whole source is 51.9±0.2 km s^{-1}. The mean velocity image shows that the higher velocities occur at the ridge of the paraboloidal structure, while the lower velocities are seen toward the tail. The average velocity of the emission integrated over the tail structure (up to 15″ behind the head's ridge) is 48.6±0.5 km s^{-1}, blueshifted by ∼4.5 km s^{-1} with respect to that of the head's ridge, 53.1±0.2 km s^{-1}. The gradient in velocity can be clearly appreciated in Figure 4,

TABLE 3

INTEGRATED H92α LINE EMISSION PARAMETERS

Source	v (km s^{-1})	Δv (km s^{-1})	S_L/S_C[a]
G13.87+0.28	51.9±0.2	22.1±0.4	0.145
G32.80+0.19A	14.0±0.4	34.4±1.1	0.0656
G32.80+0.19B	15.7±0.2	28.2±0.4	0.0871
G61.48+0.09B1	28.4±0.2	25.6±0.5	0.0936
G61.48+0.09B2	18.1±0.5	26.9±1.4	0.117

[a] Line-to-continuum ratio of flux densities.

which shows position-velocity diagrams along directions parallel (P.A. 15°, labeled ||) and perpendicular (P.A. ~75°; labeled ⊥) to the symmetry axis. These diagrams were produced by averaging the line emission over 2".8 and 2".1 wide strips, respectively; their positions are illustrated with solid lines in the top panel of Figure 1. The parallel strip shows that the velocity of the peak emission changes along the symmetry axis, decreasing from ~53 km s^{-1} at the head's ridge to ~45 km s^{-1} at the tail's edge. On the other hand, the perpendicular strip shows that the velocity of the peak emission is approximately constant across the head structure, with a mean value of 53.6 km s^{-1}.

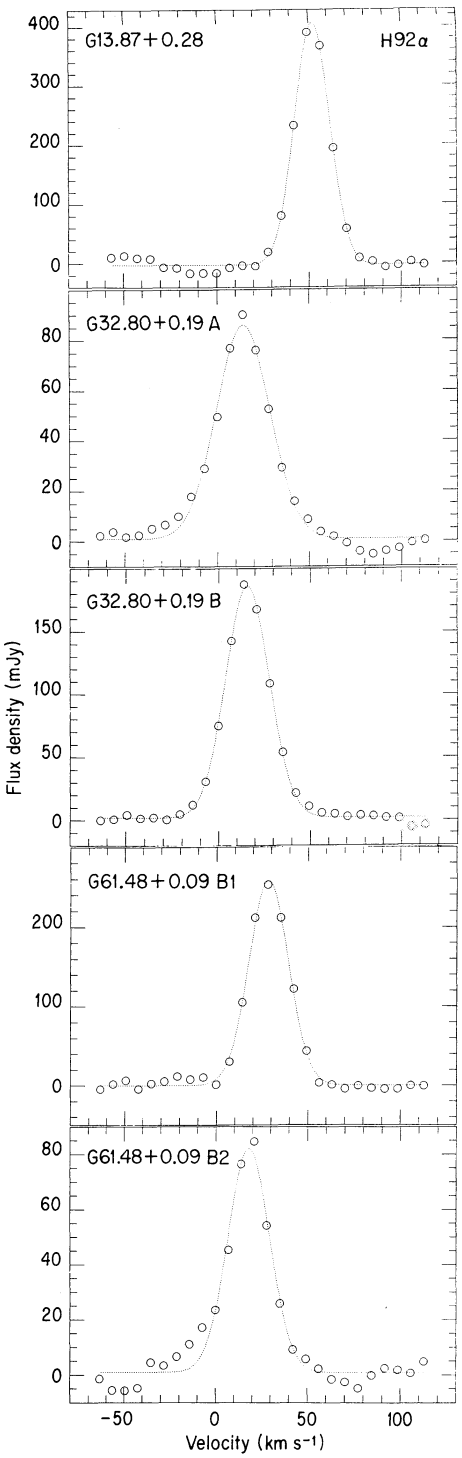

FIG. 2.—Profiles of the integrated H92α line emission from each individual H II region. *From top to bottom:* Spectra of G13.87+0.28, G32.80+0.19A, G32.80+0.19B, G61.48+0.09B1, and G61.48+0.09B2.

Line widths.—The FWHM line width of the H92α emission integrated over the whole source is 22.1±0.4 km s^{-1}, the smallest among the H II regions studied here. The velocity dispersion image shows that the line profiles are broader at the ridge of the head structure and that they decrease toward the tail. Slices of the velocity-integrated line emission and of the velocity dispersion images along the two directions shown in the top panel of Figure 1 are presented in Figure 5. While the perpendicular slice shows that the width of the emission along the head structure is approximately constant (Δv ~20 km s^{-1}), the parallel slice shows that line width steadily decreases toward the tail structure, Δv reaching a value of ~12 km s^{-1} approximately 13" behind the head's ridge. In addition, the parallel slice shows that the line width reaches its maximum value at the leading edge of the head structure. We note that the sharp decrease in line width at the edges is an artifact produced by the low signal-to-noise ratio at the borders of the H II regions.

3.2.2. *G32.80±0.19*

Individual line maps of the H92α emission from G32.80+0.19 are presented in Figure 6. Line emission was detected in the velocity range from −35.3. to 56.2 km s^{-1}. Gray-scale displays of the mean velocity and velocity dispersion images, superposed on contour plots of the velocity-integrated line emission, are presented in Figure 7.

Center velocities.—The central velocities of the integrated H92α line emission from components A and B are 14.0±0.4 and 15.7±0.2 km s^{-1}, respectively. Apparent from Figure 7*a* is a gradient in the mean velocity of the cometary-like component roughly along its symmetry axis (P.A. ~38°); the mean velocity increases from ~14 km s^{-1} in the southwest (head's leading edge) to ~23 km s^{-1} in the northeast (tail's edge). The velocity gradient can be clearly appreciated in Figure 8, which shows position-velocity diagrams along directions parallel (P.A. 38°; labeled ||) and perpendicular (P.A. −52°; labeled $\perp_1$ and $\perp_2$) to the symmetry axis. These diagrams were produced by averaging the line emission over 2".1 wide strips. The positions of the strips are illustrated as solid lines in the middle panel of Figure 1. The parallel strip shows a shift in velocity, along the cometary region, of ~9.6 km s^{-1} over an angular distance of ~10" (~0.6 pc at a distance of 13 kpc). The perpendicular strips, on the other hand, show that the velocity of the peak emission is approximately constant along directions orthogonal to the symmetry axis. The value of the constant increases as the distance from the head position increases—as expected if the flow is along the symmetry axis—being ~14.2 km s^{-1} along the perpendicular strip closer to the head ($\perp_1$) and 21.2 km s^{-1} along the perpendicular strip farther away ($\perp_2$). The velocity of the peak emission from component A is approximately constant, with an average value of ~14 km s^{-1} (see Fig. 8, *top panel*).

Line widths.—The FWHM line width of the integrated H92α emission from component A is 34.4±1.1 km s^{-1}, while that from component B is 28.2±0.4 km s^{-1}. The difference in line widths between these components is clearly appreciated in the gray-scale image (see Fig. 7*b*), which also shows that there is a smooth change in the line width along the symmetry axis of the

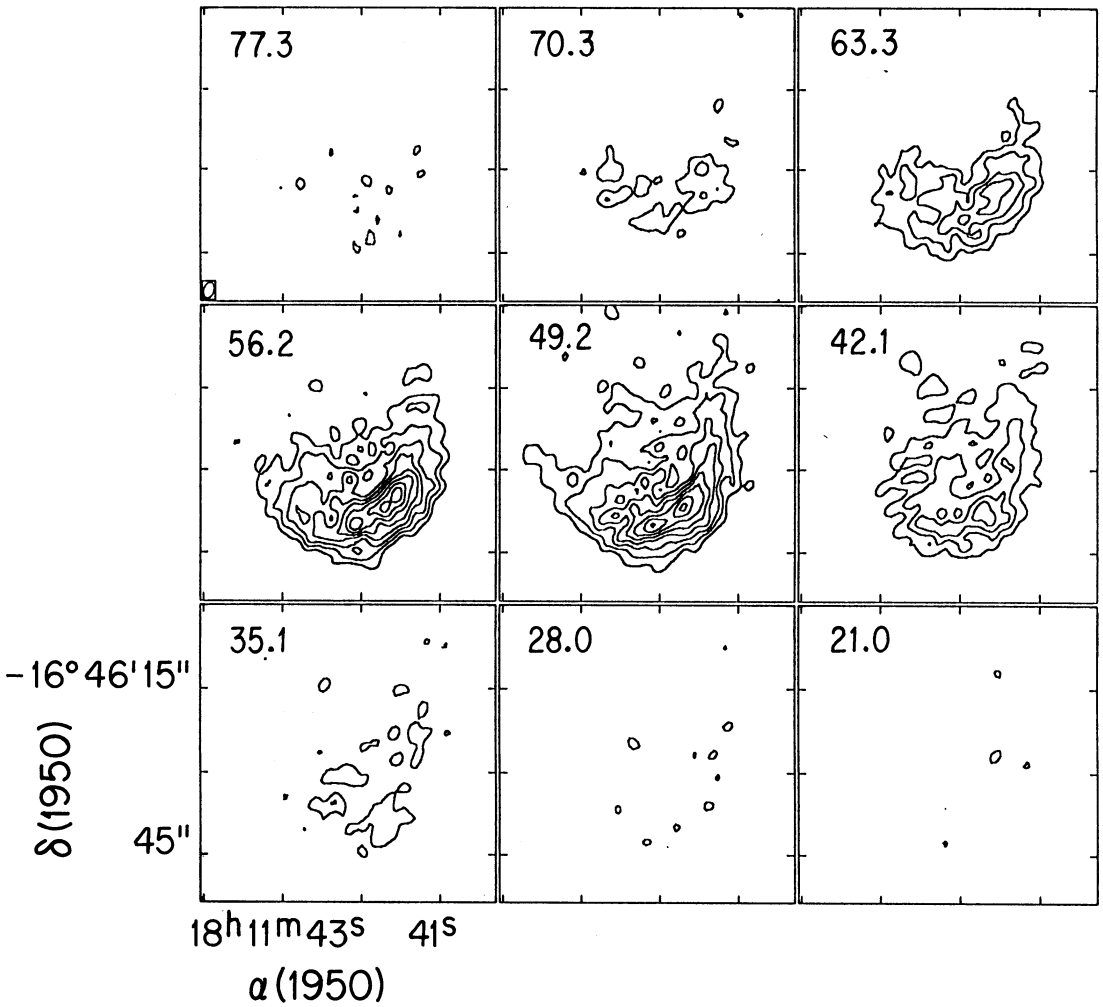

FIG. 3.—Line maps of the H92α emission from G13.87+0.28. The LSR velocity, in km s^{-1}, is indicated in the top left-corner of each line map. Contour levels are −1, 1, 2, 3, 4, 5, 6, 7, and 8 mJy beam^{-1}. The (1 σ) rms noise in the line maps is 0.32 mJy beam^{-1}. The angular resolution is 2.″9 × 1.″9 (P.A. −19°).

cometary region. The FWHM line width decreases from ∼27 km s^{-1} at the head position to ∼13 km s^{-1} at the edge of the tail. The gradient in the line width is clearly appreciated in the bottom panel of Figure 9, which shows one-dimensional slices of the three moment images along the line parallel to the symmetry axis illustrated in the middle panel of Figure 1.

3.2.3. *G61.48+0.09*

Individual line maps of the H92α emission from G61.48±0.09 are presented in Figure 10. Line emission was detected in the velocity range from −7.2 to 49.2 km s^{-1}.

Center velocities.—The central velocity of the integrated H92α line emission is 28.4±0.2 km s^{-1} for component B1 and 18.1±0.5 km s^{-1} for component B2. The mean velocity image shows that the velocity of the emission from component B1 varies with position, exhibiting a gradient roughly in an east-west direction. This gradient can be appreciated in Figure 11, which shows position-velocity diagrams along directions parallel (P.A. −80°; labeled ∥) and perpendicular (P.A. 10°; labeled $\perp_1$ and $\perp_2$) to the symmetry axis of the cometary region B1. These diagrams were produced by averaging the line emission over 2.″1 wide strips; their positions are illustrated with solid lines in the bottom panel of Figure 1. The parallel diagram shows a remarkable change in the velocity of the peak emission along the cometary region; it increases from ∼21 km s^{-1} at the leading edge of the head structure to ∼33 km s^{-1} at the tail's edge. It also shows that the gradient in velocity is steeper at the head's ridge and that it declines toward the tail. The perpendicular position-velocity diagrams (see Fig. 11, *middle and bottom panels*) show that the line-center velocities are approximately constant in directions orthogonal to the symmetry axis. The value of the constant increases as the distance from the head position increases—as expected if the flow is in a perpendicular direction—being 21.2 km s^{-1} along the perpendicular strip closer to the head ($\perp_1$) and 31.6 km s^{-1} along the perpendicular strip farther away ($\perp_2$). The velocity of the peak emission throughout component B2 is, on the other hand, approximately constant, with a value of ∼19.6 km s^{-1}.

Line widths.—The FWHM widths of the H92α emission integrated over the source are 25.6±0.5 and 26.9±1.4 km s^{-1} for components B1 and B2, respectively. Although the average line widths are similar, the velocity dispersion image shows that the individual profiles of the H92α line emission from the central region of component B2 are noticeably broader than those from component B1. The difference in the individual line widths from components B1 and B2 can be clearly appreciated

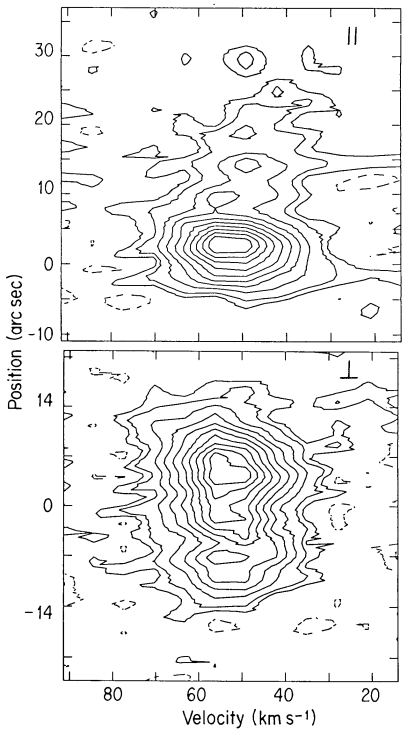

FIG. 4.—Position-velocity diagrams of the H92α emission from G13.87+0.28. *Top:* Diagram along a direction at P.A. 15° passing through $\alpha = 18^h11^m41^s.71$, $\delta = -16°46'37''.1$ (parallel strip). Contour levels are −5, 5, 10, 20, 30, 40, 50, 60, 70, 80, and 90% of the peak line brightness of 8.0 mJy beam^{-1}. *Bottom:* Diagram along a direction at P.A. −75° passing through $\alpha = 18^h11^m41^s.72$, $\delta = -16°46'36''.4$ (perpendicular strip). Contour levels are −5, 5, 10, 20, 30, 40, 50, 60, 70, 80, and 90% of the peak line brightness of 8.2 mJy beam^{-1}.

in the bottom panel of Figure 12, which shows one-dimensional slices of the three moment images along a line at P.A. −80, through $\alpha = 19^h44^m42^s.68$, $\delta = 25°05'21''.2$. The line widths within the cometary region are approximately constant, although they increase slightly from the ridge toward the tail.

4. DISCUSSION

4.1. *Morphologies*

As noted by Wood & Churchwell (1989), the morphological classification of compact H II regions is not always straightforward but depends upon resolution and sensitivity as well as on subjective judgment. For instance, Fey et al. (1992) suggest that several H II regions classified as of cometary shape may be shell sources in which the emission from one edge of the shell dominates the emission from the weaker edge. Based on their overall morphology, which shows bright emission at one edge (head) of a symmetric structure and diffuse emission behind the head, Garay et al. (1993) classified G13.87+0.28, G32.80+0.19B, and G61.48+0.09B1, as bona fide cometary H II regions.

Our 8.3 GHz continuum images show, however, that there are differences in the detailed characteristics of the brightness distribution from these cometary regions. Limb brightening of the leading edge of the ionization front is an appreciable feature only for the G13.87+0.28 region. The morphology of G32.80+0.19B at 8.3 GHz is that of a bright, arclike head with a low-brightness tail that flares away from the axis of symmetry. The brightness from G61.48+0.09B1 is strong on one side of the source (head) and decreases smoothly toward the opposite direction (tail), but does not show limb brightening. The detailed characteristics of the morphologies of these two cometary-like H II regions argue against the bow shock interpretation, which predicts limb brightening, and that the brightness should taper away from the symmetry axis.

4.2. *Derived Parameters*

In this section we will make use of the observed quantities averaged over the source and therefore will derive physical parameters appropriate to the bulk of the H II region.

4.2.1. *Recombination Line*

Our observations of the H92α recombination line allow us to estimate the electron temperature of the H II regions. Assuming that the ionized gas is in local thermodynamic equilibrium, the electron temperature, T_e^*, is given by

$$T_e^* = 2.21 \times 10^3 \left(\frac{\nu}{\mathrm{GHz}}\right)^{0.96} \left(\frac{S_L}{S_C}\right)^{-0.87} \left(\frac{\Delta v}{\mathrm{km\ s^{-1}}}\right)^{-0.87} \times (1 + y^+)^{-0.87}\ \mathrm{K}\,, \quad (1)$$

where S_L/S_C is the line-to-continuum ratio of flux densities, Δv is the observed line width (FWHM), ν is the frequency of the line, and y^+ is the number ratio of singly ionized helium to ionized hydrogen. The LTE temperatures are given in column (2) of Table 4.

The LTE temperatures may not, however, be a reliable estimate of the true electron temperature. For a wide range of electron densities and electron temperatures, stimulated effects produce an enhancement of the line and consequently an enhancement of the line-to-continuum ratio (cf. Brown, Lockman, & Knapp 1978). The deviations increase with the continuum opacity (Goldberg 1968); thus, among nebulae with similar values of n_e and T_e, the enhancement is more important for those which have the larger emission measures.

In order to assess the importance of stimulated emission for the H II regions studied here we computed non–LTE models for the H92α line. Using the full solution of the transfer equation, the line-to-continuum ratio for an isothermal, homogeneous, nebula is given by (cf. van Gorkom et al. 1980)

$$\frac{T_L}{T_C} = \left(\frac{\tau_C + b\tau_L^*}{\tau_C + b\beta\tau_L^*}\right)\left\{\frac{1 - \exp\left[-(b\beta\tau_L^* + \tau_C)\right]}{1 - \exp\left(-\tau_C\right)}\right\} - 1\,, \quad (2)$$

where τ_C is the continuum optical depth, τ_L^* is the peak line optical depth assuming LTE, and b and β are the usual departure coefficients from LTE (Brocklehurst 1970). The line-to-continuum ratio is a function, through τ_C, τ_L^*, b, and β, of the nebular parameters electron temperature, electron density, path length, and Doppler width of the recombination line. Thus, in general, a range of electron temperatures, electron

TABLE 4

ELECTRON TEMPERATURES

Source (1)	T_e^* (K) (2)	T_e (K) (3)	T_e/T_e^* (4)
G13.87+0.28	5700	7000	1.2
G32.80+0.19A	7700	16000	2.1
G32.80+0.19B	7100	10000	1.4
G61.48+0.09B1	7300	10000	1.4
G61.48+0.09B2	5700	9000	1.6

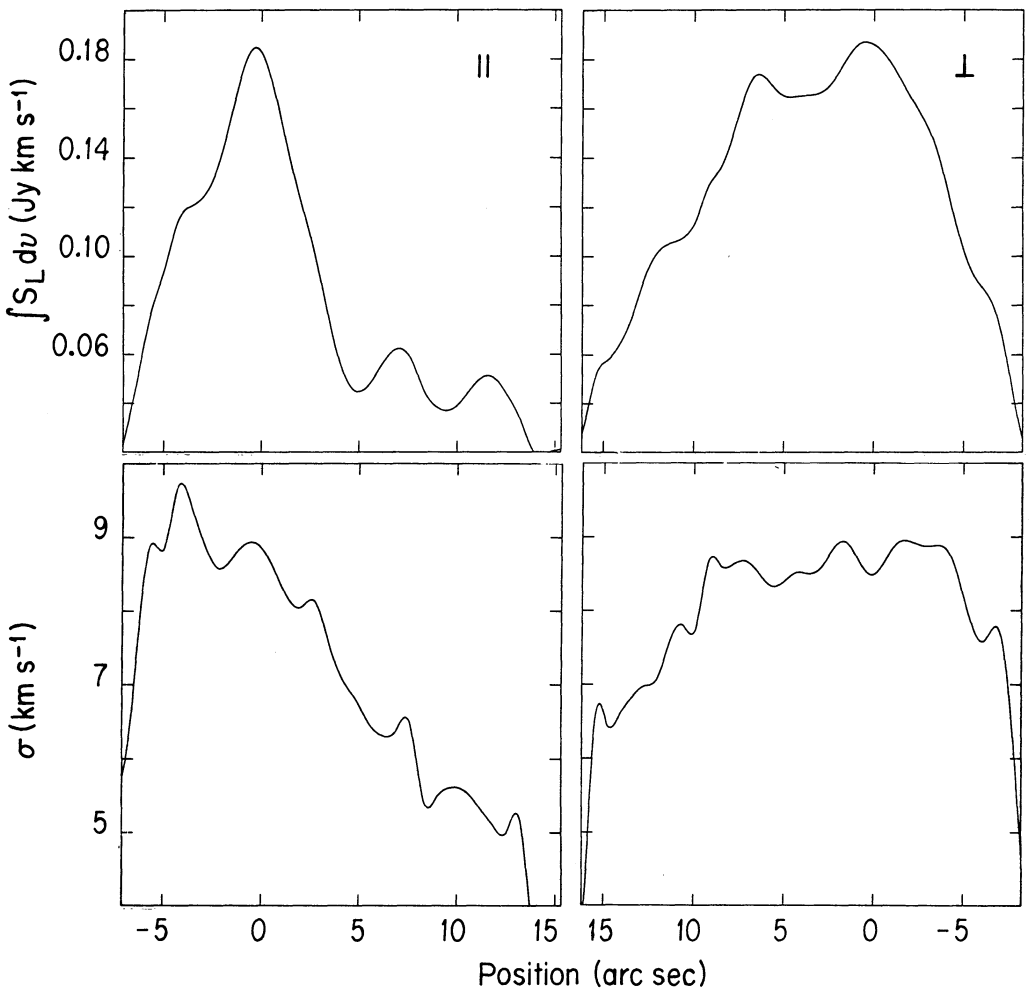

FIG. 5a FIG. 5b

FIG. 5.—One-dimensional slices of moments of the H92α emission from G13.87+0.28. (*a*) Slices through $\alpha = 18^h11^m41^s.88$, $\delta = -16°46'33''.4$ at a position angle of 15° (parallel). *Top:* zero-order moment (velocity-integrated emission); *bottom:* second-order moment (velocity dispersion). (*b*) Slices through $\alpha = 18^h11^m41^s.95$, $\delta = -16°46'38''.8$ at a position angle of −75° (perpendicular). *Top:* zero-order moment; *bottom:* second-order moment.

densities, and path lengths can reproduce the observed ratio. Fortunately, constraints on these parameters are provided by the observed radio continuum spectra (see § 4.2.2) and by the observed angular size. The line width imposes an additional constraint on the electron density through pressure broadening (Brocklehurst & Leeman 1971).

Using an iterative procedure to reproduce the observed line-to-continuum ratio, the radio continuum spectra, and the line width, we derive the electron temperatures given in column (3) of Table 4. The values of b and β were computed by interpolation in the tables given by Brocklehurst & Seaton (1972). Pressure broadening of the line was taken into account using the approximation of van Gorkom et al. (1980). The T_e/T_e^* ratios, given in column (4) of Table 4, range between 1.2 and 2.1, showing that non-LTE effects at the frequency of the H92α line are important for the H II regions considered here. Shaver (1980) found that for a given emission measure there is a unique frequency given by $\nu \sim 0.081\ \mathrm{EM}^{0.36}$, where ν is in GHz and EM is in pc cm^{-6}, at which $T_e/T_e^* = 1$. Hence, at the frequency of 8.3 GHz non-LTE effects are negligible only for H II regions with $\mathrm{EM} \sim 4 \times 10^5$ pc cm^{-6}. Within the range of emission measures spanned by the sources studied here ($2 \times 10^6 \leq \mathrm{EM} \leq 2 \times 10^8$ pc cm^{-6}) Shaver (1980) finds that T_e/T_e^* ranges between 1.1 and 2.1, in very good agreement with the ratios derived by us. As expected, the ratios are significantly correlated with the emission measures, the higher ratios being found for the H II regions with the higher emission measures. We conclude that for the H92α line the LTE approximation is not a good assumption for the sources investigated here, particularly for those with the highest emission measures.

4.2.2. *Radio Continuum*

For a homogeneous H II region, with an electron temperature T_e, the flux density at frequency ν is given by

$$\left(\frac{S_\nu}{\mathrm{Jy}}\right) = 7.222 \times 10^{-3}\left(\frac{\nu}{\mathrm{GHz}}\right)^2\left(\frac{T}{10^4\ \mathrm{K}}\right)\left(\frac{\Omega_{\mathrm{BB}}}{\mathrm{arcsec}^2}\right) \times [1 - \exp(-\tau_\nu)]\,, \quad (3)$$

where Ω_{BB} is the solid angle of the source at optically thick frequencies,

$$\tau_\nu = 0.08235\left(\frac{\mathrm{EM}}{\mathrm{pc\ cm^{-6}}}\right)\left(\frac{\nu}{\mathrm{GHz}}\right)^{-2.1}\left(\frac{T_e}{10^4\ \mathrm{K}}\right)^{-1.35}$$

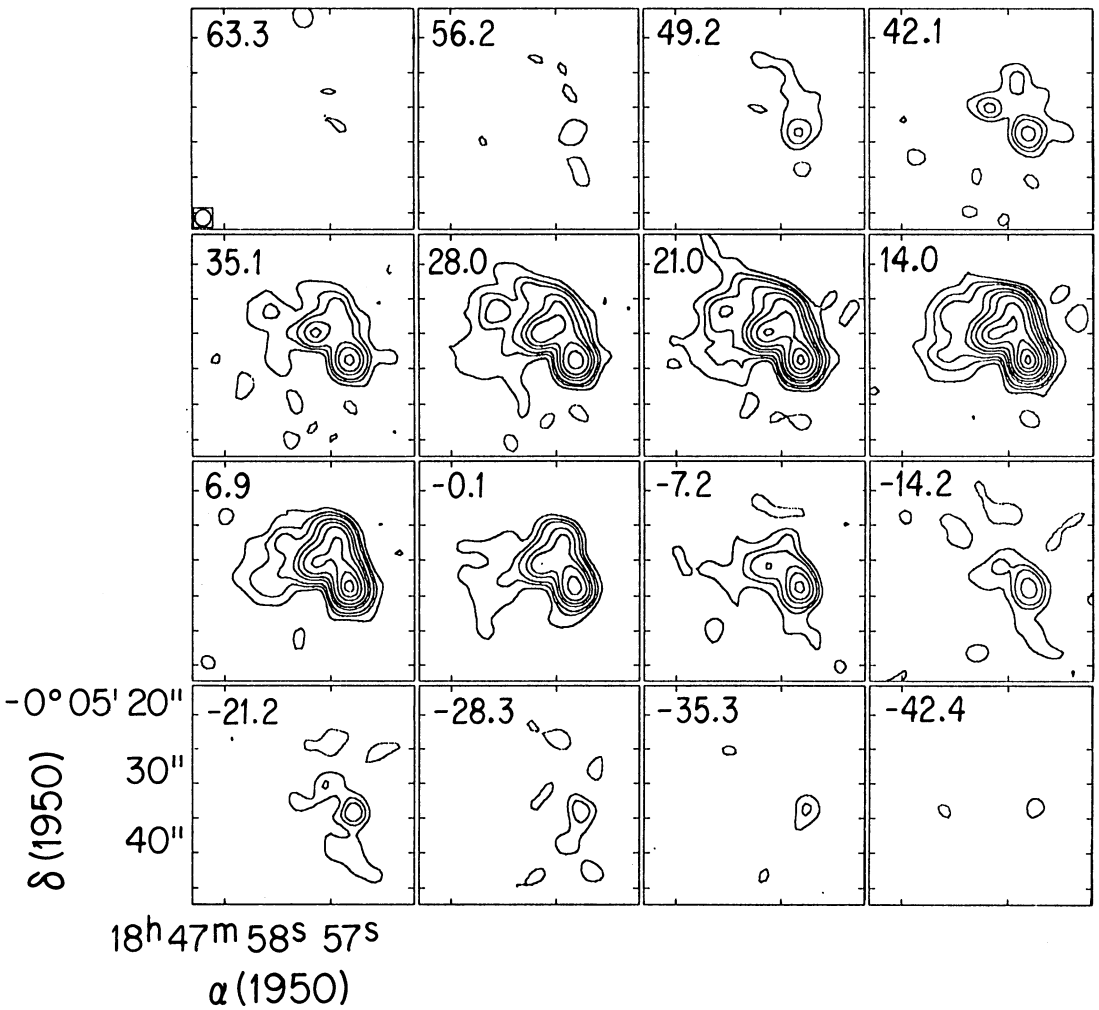

FIG. 6.—Line maps of the H92α emission from G32.80+0.19. The LSR velocity, in km s^{-1}, is indicated in the top left-hand corner of each line map. Contour levels are −1, 1, 2, 3, 5, 7, 10, 15, 20, 25, and 30 mJy $beam^{-1}$. The (1 σ) rms noise in the line maps is 0.32 mJy $beam^{-1}$. The angular resolution is 2.″3 × 2.″2 (P.A. −25°).

is the optical depth averaged over the source angular size, and EM is the emission measure. Thus, assuming that the electron temperature is known, the measurement of the continuum spectra over a range of optically thick and thin frequencies allows one to determine the emission measure and the *effective blackbody* solid angle of the H II region.

The radio continuum spectra of the H II regions, constructed using all known interferometric measurements of the flux density, are shown in Figure 13. The solid line corresponds to the theoretical spectrum of a homogeneous, constant-density H II region, computed using the values of T_e, Ω_{BB}, and EM that resulted from the simultaneous fitting of the observed continuum spectra, line-to-continuum ratio, angular size, and line width. The values of the fitted parameters are given in Table 5.

TABLE 5

DERIVED PARAMETERS OF H II REGIONS

Source (1)	D[a] (kpc) (2)	Ω_{BB} (arcsec^2) (3)	EM (pc cm^{-6}) (4)	L (pc) (5)	n_e (cm^{-3}) (6)	τ_C (7)	N_i (s^{-1}) (8)
G13.87+0.28	4.4	826	2.0×10^6	0.85	1.5×10^3	0.01	7.7×10^{48}
G32.80+0.19A	13.0	5.5	1.6×10^8	0.20	2.7×10^4	0.3	1.9×10^{49}
G32.80+0.19B.....	13.0	137	9.0×10^6	1.0	2.9×10^3	0.04	3.8×10^{49}
G61.48+0.09B1	5.4	290	7.2×10^6	0.62	3.2×10^3	0.03	1.1×10^{49}
G61.48+0.09B2	5.4	14	3.1×10^7	0.13	1.5×10^4	0.1	2.5×10^{48}

[a] Taken from Churchwell et al. 1990.

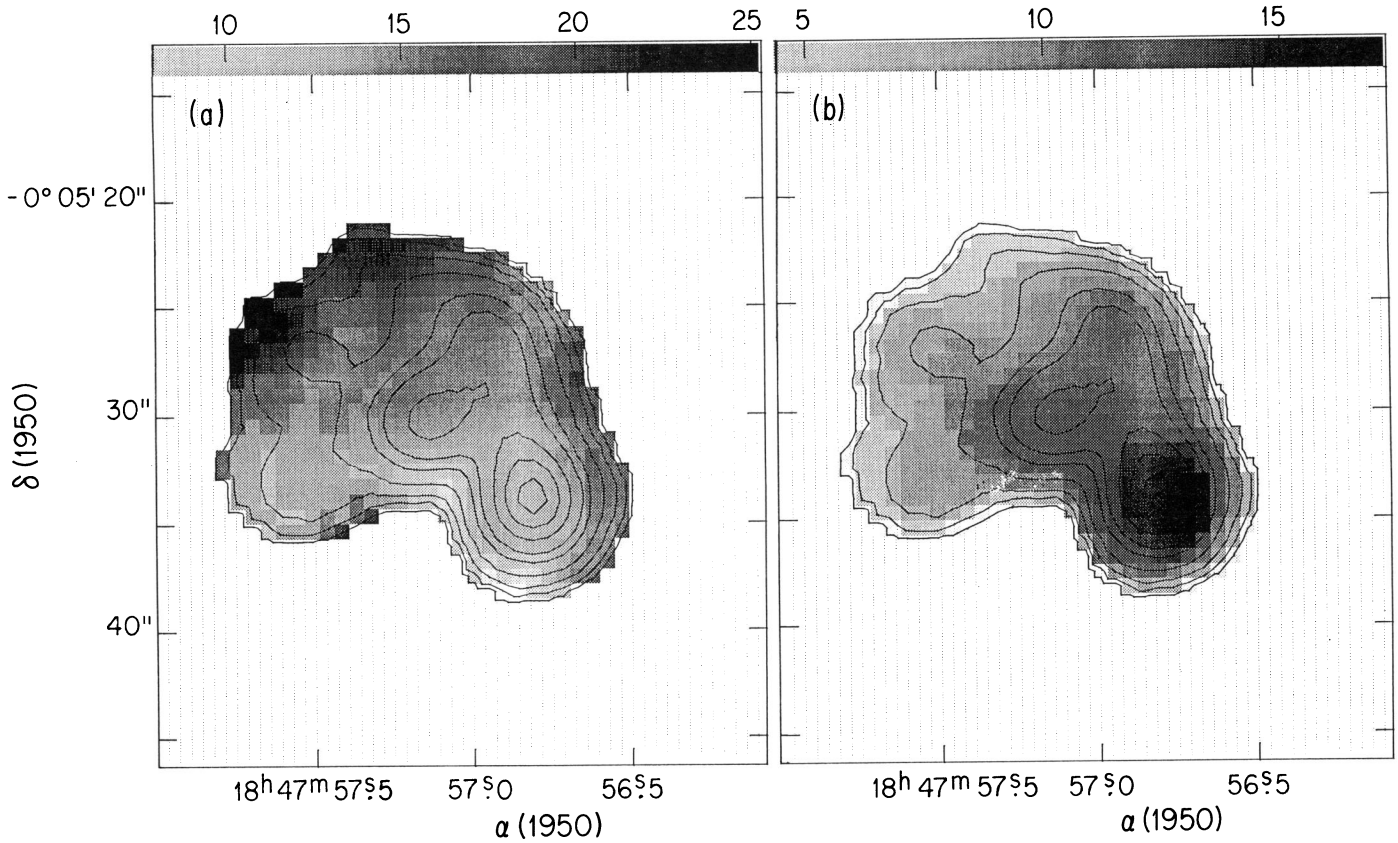

FIG. 7.—Gray-scale maps of moments of the H92α emission from G32.80+0.19, superposed on contour plots of the velocity-integrated line emission. (*a*) first-order moment (mean velocity) map. Gray scale ranges from 8 to 25 km s^{-1}. (*b*) second-order moment (velocity dispersion) map. Gray scale ranges from 5 to 17 km s^{-1}.

The electron densities, given in column (6) of Table 5, were computed from the emission measures using the relation $n_e = [\mathrm{EM}/(1 + y^+)L]^{1/2}$, where L is the path length along the line of sight, estimated as $L = (6\Omega_{BB}/\pi)^{1/2}D$, and D is the distance to the source (given in col. [2]). The optical depth at 8.3 GHz, τ_C, and the number of ionizing photons needed to excite the H II region, N_i, are given in columns (7) and (8), respectively.

4.3. *Clustering*

Two of our cometary sources, G32.80+0.19B and G61.48+0.09B1, are found projected within short distances (~0.4 pc) of compact H II regions. This is not an uncommon situation; a large fraction of the classified cometary regions are found near other compact H II regions (cf. Wood & Churchwell 1989). As mentioned by Fey et al. (1992), the close location of the cometary H II regions to other compact H II regions and their location in the densest part of the molecular cloud argues against the bow shock model. For instance, assuming that an O star is formed with a velocity of 10 km s^{-1} relative to its natal molecular cloud, during its lifetime (~10^6 yr) it will be carried ~10 pc away from its birthplace. Thus, bow shock cometary H II regions are expected to be found isolated within molecular clouds.

4.4. *Dynamics of the Ionized Gas*

In this section we summarize the observed kinematics of the cometary regions of ionized gas (H92α velocity and line width) and of the molecular gas associated to them (NH_3 and CO velocities), and discuss their dynamical relationship. Appropriate comparisons are made with the predictions of the champagne and bow shock models. Regarding this point, we notice that, in addition to the differences in the relative motions between the ionized and molecular gas and in the velocity gradients mentioned in § 1, there is a further significant difference between the model predictions concerning line widths. The bow shock model predicts that the line widths of the recombination lines should exhibit broadenings of the order of the velocity of the star with respect to the molecular cloud and that the line widths along the leading edge of the ionization front should be broader than behind it (Van Buren & Mac Low 1992). On the other hand, the champagne phase model calculations show that the line profiles are asymmetric and broader in the tail region (Yorke, Tenorio-Tagle, & Bodenheimer 1984).

To date there are no champagne models that include the effects of the powerful stellar winds characteristic of high-mass stars. This is an important project that should be undertaken. Nevertheless, in the Appendix we investigate in a simple fashion under which conditions the stellar wind remains confined inside the champagne flow, ensuring that this dominates the dynamics of the ionized gas. Under the assumption that the stellar wind is turned on in a very early stage of the star's evolution, once the champagne flow has already started, we find that for typical values of molecular densities within cloud cores and expected stellar wind parameters the wind remains confined inside the champagne flow. Hence, we conclude that, to a first approximation, it is permissible to compare the observed velocity field of cometary H II regions with the predictions of currently available champagne models.

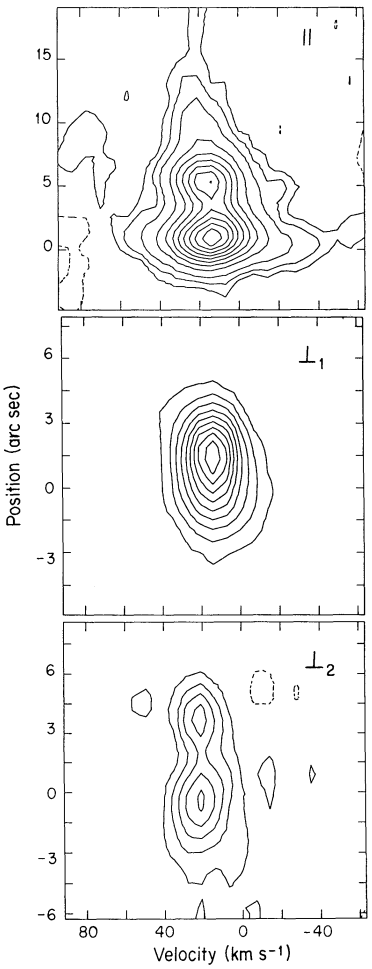

FIG. 8.—Position-velocity diagrams of the H92α emission from G32.80+0.19. *Top:* Diagram along a direction at P.A. 38° passing through $\alpha = 18^h47^m57^s.02$, $\delta = -0°05'29''.5$ (parallel strip). Contour levels are −2.5, 2.5, 5, 10, 20, 30, 40, 50, 60, 70, 80, and 90% of the peak line brightness of 29.7 mJy beam^{-1}. *Middle:* Diagram along a direction at P.A. −52° passing through $\alpha = 18^h47^m56^s.98$, $\delta = -0°05'30''.4$ (perpendicular strip at head's leading edge, $\perp_1$). Contour levels are −10, 10, 20, 30, 40, 50, 60, 70, 80, and 90% of the peak line brightness of 19.5 mJy beam^{-1}. *Bottom:* Diagram along a direction at P.A. −52° passing through $\alpha = 18^h47^m57^s.51$, $\delta = -0°05'25''.9$ (perpendicular strip at tail, $\perp_2$). Contour levels are −15, 15, 30, 45, 60, 75, and 90% of the peak line brightness of 6.3 mJy beam^{-1}.

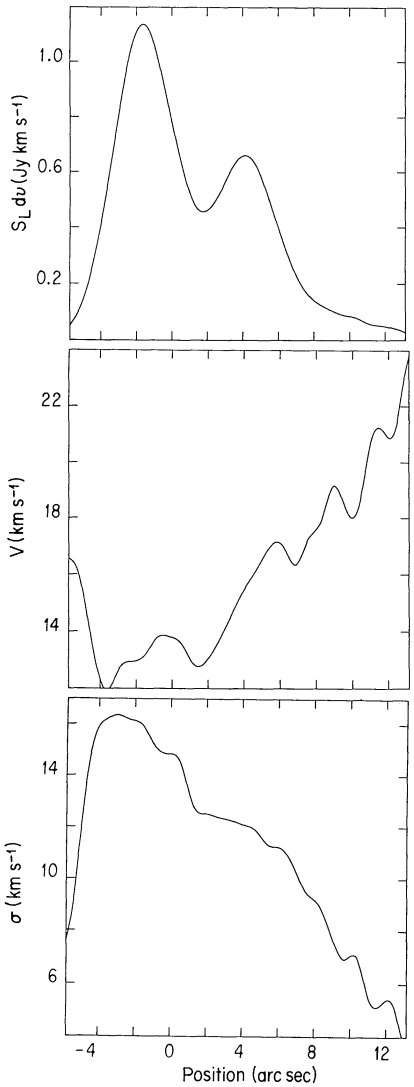

FIG. 9.—One-dimensional slices of moments of the H92α emission from G32.80+0.19, through $\alpha = 18^h47^m57^s.06$, $\delta = -0°05'30''.0$ (central position) at P.A. 38°. *Top:* Slice of zero-order moment (velocity-integrated emission) image. *Middle:* Slice of first-order moment (mean velocity) image. *Bottom:* Slice of second-order moment (velocity dispersion) image.

4.4.1. *G13.87+0.28*

Observations of the (1, 1) and (2, 2) lines of NH_3 show that the velocity of the molecular toward G13.87+0.28 is 48.4±0.5 km s^{-1} (Churchwell, Walmsley, & Cesaroni 1990). The presence of excited molecular gas at a higher velocity is indicated by the detection of emission in the (4, 4) inversion transition of NH_3 having a line-center velocity of 50.3±0.4 km s^{-1} (Cesaroni, Walmsley, & Churchwell 1992). The difference in velocity between the low- and high-excitation lines of ammonia, ∼2 km s^{-1}, is statistically significant, suggesting that the excited ammonia emission arises from a slightly different region. Our observations show that the average velocity of the ionized gas in the head of G13.87+0.28 is ∼53.1±0.2 km s^{-1}, while that in the tail region is ∼48.6±0.5 km s^{-1}.

The velocity and line-width fields observed toward G13.87±0.28 are consistent with the bow shock model, which correctly predicts that the velocity in the tail should be similar to the molecular cloud velocity and that the line widths should be broader at the ridge of the head structure. A comparison of the observed radio continuum and velocity-position maps with the bow shock model maps at various inclinations presented by Van Buren & Mac Low (1992) suggests that the star is moving at an angle ∼60° with respect to the line of sight. We note, however, that the observed velocity behavior is not as clear as in the model maps which were computed using a speed of 50 km s^{-1}. The actual velocity of the exciting star relative to the molecular cloud, v_*, is unknown, and is difficult to estimate, but it is probably smaller than the model value (see discussion below). An additional piece of evidence supporting the bow shock model in this source is provided by the presence of excited molecular emission which is redshifted with respect to the velocity of the cool molecular cloud (as is the ionized gas in the head), suggesting that the excited NH_3 emission arises from the swept-up shocked molecular gas.

The bow shock hypothesis to explain the morphology and

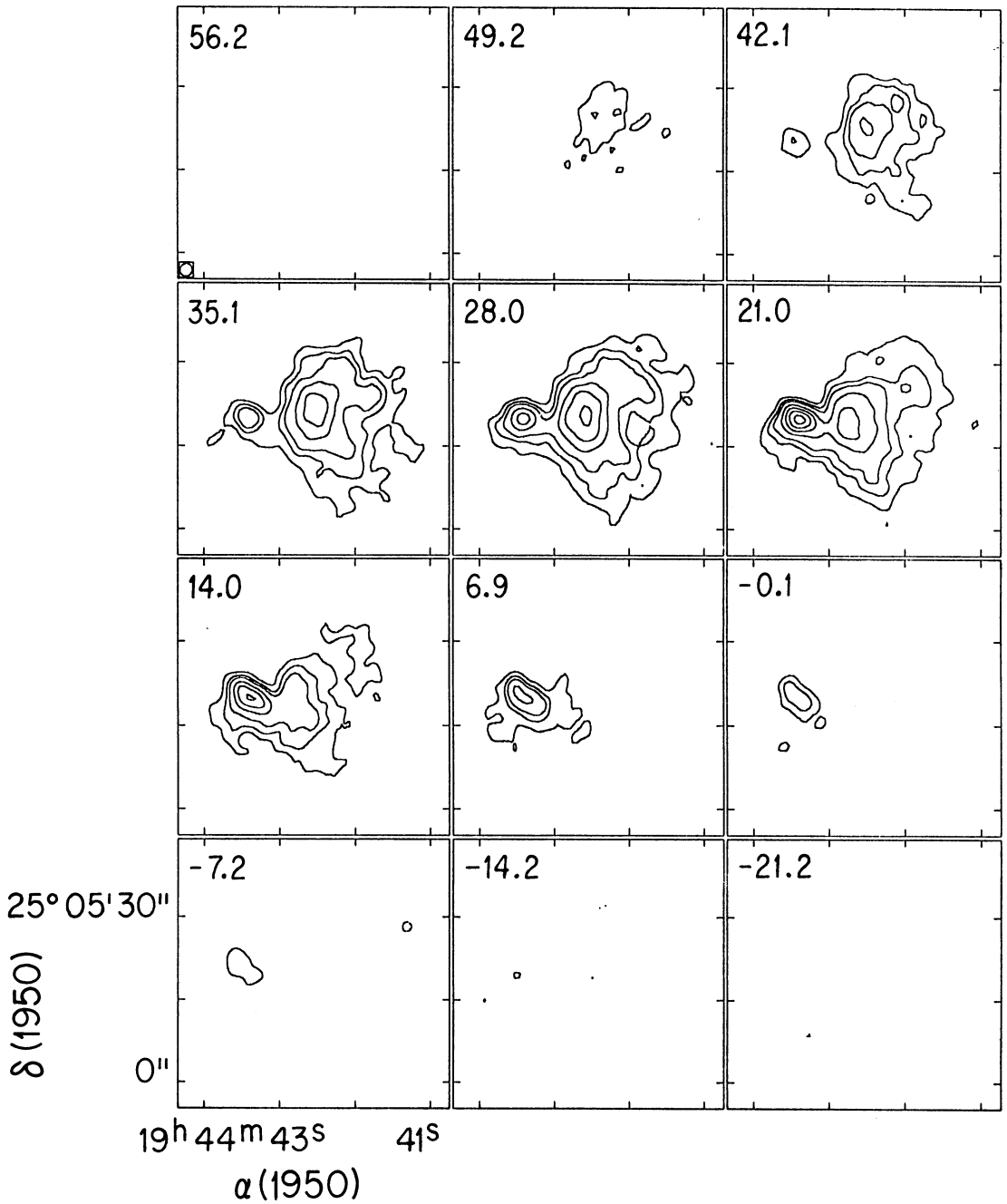

FIG. 10.—Line maps of the H92α emission from G61.48+0.09. The LSR velocity, in km s^{-1}, is indicated in the top left-hand corner of each line map. Contour levels are −1, 1, 2, 3, 5, 7, 9, and 11 mJy beam^{-1}. The (1 σ) rms noise in the line maps is 0.25 mJy beam^{-1}. The angular resolution is 2.″4 × 2.″1 (P.A. −24°).

velocity structure of the cometary G13.87+0.28 region is not free of shortcomings, however. For instance, the observed line widths in the hand structure are quite narrow, ~22 km s^{-1}. An upper limit to v_* can be obtained from the observed line width as follows: Assuming that the broadening of the line is produced by thermal and microturbulent motions, we find, using expression (2) of Garay (1990) with $T_e = 7000$ K, a FWHM turbulent width Δv_t of ~13 km s^{-1}. Further, if we assume that the turbulent motions of the ionized gas are mainly produced by the passage of the bow shock, then $\Delta v_t \sim v_*$ (Hartigan, Raymond, & Hartmann 1987), implying that $v_* \sim 13$ km s^{-1}. This value corresponds, however, to an upper limit on the stellar velocity, since part of the turbulent width is likely to be produced by microturbulent motions that are independent of the star motion and which are observed to be of this order in normal H II regions (e.g., Garay & Rodríguez 1983). Therefore, one should expect broader lines in bow shock models.

4.4.2. *G32.80+0.19*

The velocity of the ambient molecular gas toward G32.80+0.19, determined from observations of the (1, 1) and (2, 2) lines of NH_3 (Churchwell et al. 1990), is 16.1 ± 0.5 km s^{-1}. Our observations show that the velocity of the ionized gas is

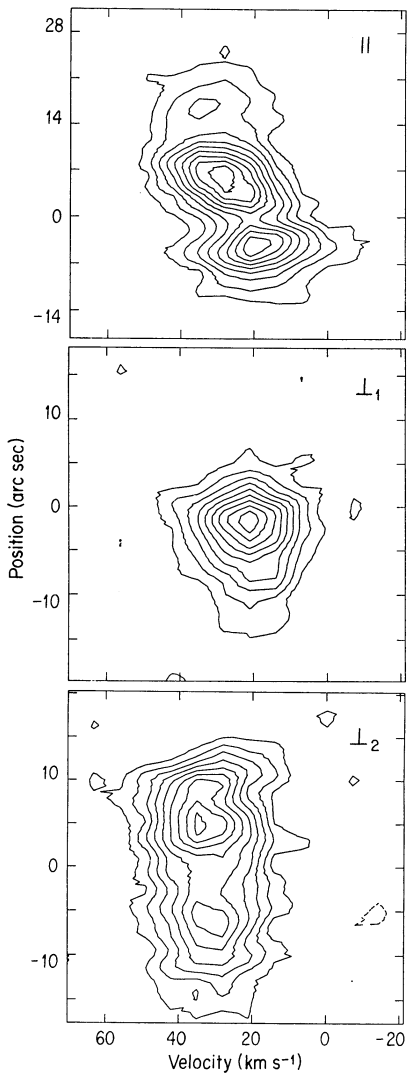

FIG. 11.—Position-velocity diagrams of the H92α emission from G61.48+0.09. *Top:* Diagram along a direction at P.A. −80° through α = 19^{h}44^{m}42^s.74, δ = 25°05′19″.6 (parallel strip). Contour levels are −10, 10, 20, 30, 40, 50, 60, 70, 80, and 90% of the peak line brightness of 9.3 mJy beam^{-1}. *Middle:* Diagram along a direction at P.A. 10° through α = 19^{h}44^{m}42^s.97, δ = 25°05′17″.7 (perpendicular strip, $\perp_1$). Contour levels are −10, 10, 20, 30, 40, 50, 60, 70, 80, and 90% of the peak line brightness of 5.7 mJy beam^{-1}. *Bottom:* Diagram along a direction at P.A. 10° through α = 19^{h}44^{m}42^s.15, δ = 25°05′22″.5 (perpendicular strip, $\perp_2$). Contour levels are −10, 10, 20, 30, 40, 50, 60, 70, 80, and 90% of a line brightness of 5.0 mJy beam^{-1}.

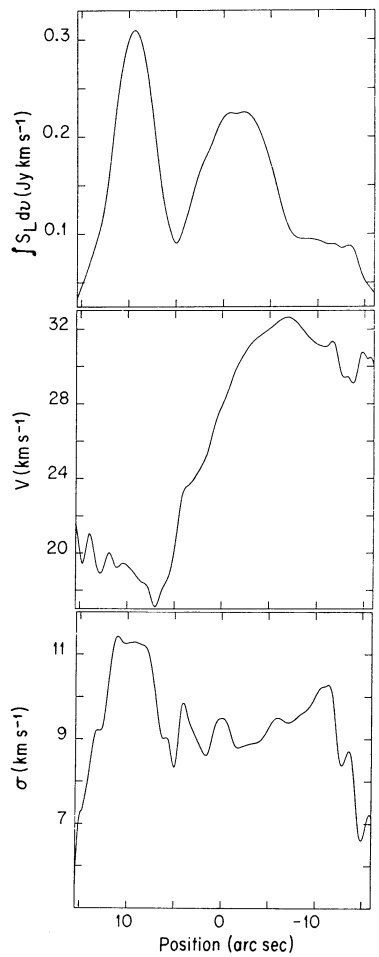

FIG. 12.—One-dimensional slices of moments of the H92α emission from G61.48+0.09 along a line at P.A. −80° through α = 19^{h}44^{m}42^s.68, δ = 25°05′21″.2. *Top:* Slice of the zero-order moment (velocity-integrated emission) image. *Middle:* Slice of the first-order moment (mean velocity) image. *Bottom:* Slice of the second-order moment (velocity dispersion) image.

~14 km s^{-1} at the head's leading edge of the cometary region and that it increases toward the tail, reaching ~22 km s^{-1} at an angular distance of ~9″ behind the head. The line widths are broader at the ridge of the head and narrower toward the tail. The velocity structure observed toward the cometary region can be accounted for by the champagne model, which rightly predicts that the velocity of the ionized gas at the head should be similar to the velocity of the associated molecular gas and that the ionized gas in the tail structure should be streaming away from the molecular cloud. We want to note, however, that a shortcoming of the champagne model interpretation is that the line width decreases along the symmetry axis (Fig. 9), a feature not predicted by a straightforward application of the model. On the other hand, this feature is predicted by the bow shock models.

The ionized gas from component A has an average velocity of ~14 km s^{-1} and an average line width of 34.4 km s^{-1}, the largest among the H II regions investigated here. The similar velocities of the ionized gas and molecular cloud, and the broad line widths, suggest that this source may be a young H II region that is deeply embedded within the molecular cloud and is undergoing expansion motions.

4.4.3. *G61.48+0.09*

Observations of the (1, 1) and (2, 2) lines of NH_3, with a beam of ~40″, show that the velocity of the molecular gas toward this source is 22.0±0.3 km s^{-1} (Macdonald et al. 1981; Churchwell et al. 1990). Observations in CO, with an angular resolution of ~22″, show a horseshoe-like distribution with the position of the peak emission lying very close to the compact H II region S88B2 (White & Fridlund 1992). The CO observations also show that there is a velocity gradient of ~1 km s^{-1} arcmin^{-1} running from northeast to southwest, the line-center velocity at the position of the compact H II regions is ~22 km s^{-1}, in good agreement with the NH_3 results.

About 35″ west of the head of the cometary radio source S88B1 there is a visible nebulosity, having an angular diameter of ~50″ and showing strong Hα emission (Deharveng & Mau-

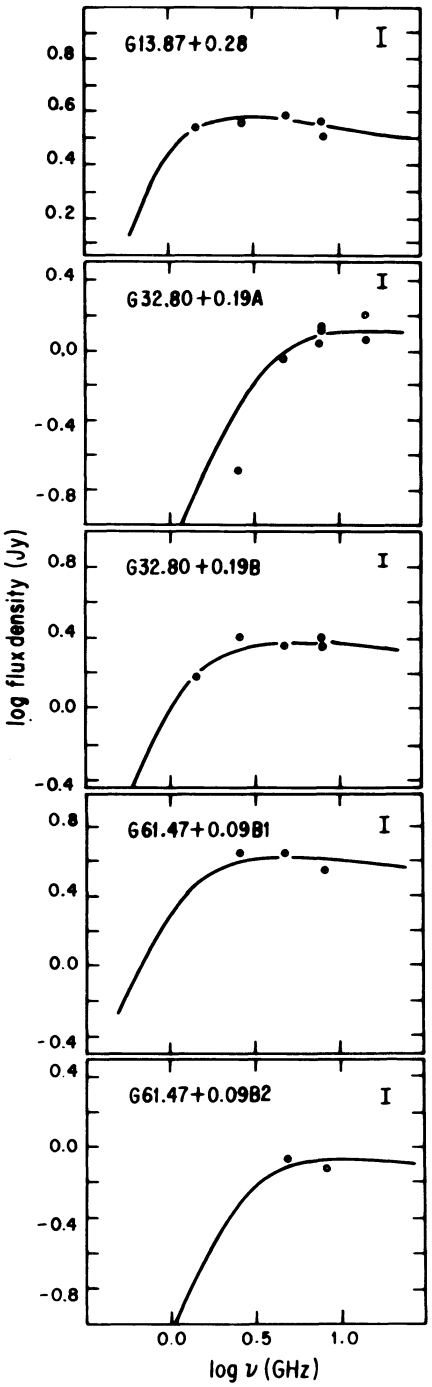

FIG. 13.—Radio continuum spectra of the individual H II regions. The solid lines correspond to theoretical spectra of homogeneous H II regions with values of the parameters T_e, Ω_{BB}, and EM, chosen as described in the text. The error bars in each panel indicate a $\pm 10\%$ accuracy in the value of the flux densities.

cherat 1978). It exhibits a considerable overlap with the tail radio structure (see Fig. 4 of Felli & Harten 1981 for an overlay of the radio and Hα emission). The Hα brightness decreases very steeply toward the head radio structure, suggesting that the head of the cometary region is deeply embedded within a molecular cloud. The sharp northeast edge of the Hα emission probably marks the edge of a dense molecular structure. The Hα velocities of the optical nebulosity associated with the western side of the radio tail are greater than 28 km s^{-1} (Deharveng & Maucherat 1978).

Our observations show that the velocity of the ionized gas is ~ 21 km s^{-1} at the head's leading edge of the cometary region and that it increases toward the tail, where it reaches ~ 33 km s^{-1}. The H92α velocities in the tail are in good agreement with the Hα velocities. The similar velocity of the ionized gas at the head's leading edge (~ 21 km s^{-1}), and of the molecular gas (~ 22 km s^{-1}) combined with the continuous gradient in the velocity of the ionized gas from the compact radio head, extended radio tail, and optical diffuse nebula, suggest that this region is undergoing a champagne flow. The ionized gas is streaming away from the molecular gas toward low-density regions, reaching a velocity of about 11 km s^{-1}, relative to the molecular gas velocity, at the edge of the tail structure. The velocities observed at the tail's edge are in agreement with the champagne model, which predicts that in the vicinity of the nozzle the velocities should approach the sound speed of the ionized gas. Even though ionized gas with higher velocities (~ 2–3 times the sound speed) is likely to be present (Yorke et al. 1984), it would probably be unobservable because of its low emission measure. Additional support for the champagne hypothesis is provided by the velocity dispersion distribution, which shows a slight increase in the value of the line width from head to tail, as predicted by the champagne models.

4.5. *G13.87+0.28 as a Bow Shock Cometary Region*

In this section we investigate whether the known properties of the exciting star of G13.87+0.28 are consistent with the bow shock hypothesis for the origin of the cometary morphology. Observational constraints on the model parameters are provided by the observed size scale of the bow shock and by the observed velocity field. We derived the standoff distance, l, of the wind shock from the star (Van Buren et al. 1990) by fitting a parabola to the shape of the outer edge of the radio continuum morphology. The parabolic shape was taken to be $y = x^2/3l$, where x and y are the coordinates perpendicular and parallel to the direction of motion. Assuming that the last is inclined with respect to the line of sight by an angle of 60° (as suggested by the observed velocity field; see § 4.4.1), we find that the symmetry axis of the parabola is at P.A. 15° and that l is $\sim 9''$, which corresponds to a linear dimension of 6×10^{17} cm at a distance of 4.4 kpc.

The standoff distance depends on the momentum rate of the stellar wind, the ambient cloud density, and the velocity of the star. None of these quantities have been determined for G13.87+0.28; thus a wide range of parameters can reproduce the observed value of l. Fortunately, radio and infrared observations yield information on the characteristics of the exciting star, which in turn provides constraints on the momentum rate of the wind. The far-infrared luminosity, in the 1–1300 μm range, is $2.2 \times 10^5\ L_\odot$ (Chini, Krügel, & Wargau 1987; distance of 4.4 kpc), while the rate of ionizing photons required to explain the observed radio continuum flux densities is 7.7×10^{48} s^{-1} (see Table 5). Both of these results can be well explained if G13.87+0.28 is excited by an O6.5 ZAMS star. Using the results of Van Buren (1985), a star with a luminosity of $2.2 \times 10^5\ L_\odot$ and an effective temperature of 40,000 K is expected to have a wind mass-loss rate, $\dot{M}_w$, of $\sim 1 \times 10^{-6}\ M_\odot$ yr^{-1} and a stellar wind velocity, v_w, of ~ 2500 km s^{-1}, implying that $\dot{M}_w v_w \sim 2.5 \times 10^{-3}\ M_\odot\ yr^{-1}$. An estimate of the hydrogen density of the ambient cloud in which the exciting star is traveling is provided by the electron density of the

ionized gas, which is derived from the radio continuum observations (see § 4.2.2). Assuming uniform conditions, we found an average rms electron density of 1.5×10^3 cm^{-3}. We note, however, that the ionized gas is likely to have density gradients, so this value is only representative of the bulk conditions. For instance, at the ridge of the cometary structure we derive a peak emission measure of 4.5×10^6 pc cm^{-6}, which, assuming a path length in the line of sight equal to the standoff distance, implies a peak electron density of 5×10^3 cm^{-3}. Hereafter, we will assume that the hydrogen density of the ambient gas toward G13.87+0.28 is 2×10^3 cm^{-3}.

Knowing the wind momentum rate, the ambient medium density, and the standoff distance, the application of the bow shock model allows us to estimate the velocity of the star relative to the ambient medium. Using equation (2) in Van Buren et al. (1990), with $\mu_H = 1.4$, $n_H = 2 \times 10^3$ cm^{-3}, and $\dot{M}_{w,-6} v_{w,8} = 2.5$, where $\dot{M}_{w,-6}$ is the wind mass-loss rate in units of $10^{-6}\ M_\odot$ yr^{-1} and $v_{w,8}$ is the stellar wind velocity in units of 1000 km s^{-1}, we find that $v_* = 8.5$ km s^{-1}. This value is consistent with the upper limit derived from the observed line width, giving support to the wind shock hypothesis. Further, by applying equation (9) of Van Buren et al. (1990), assuming $T_{II,4} = 0.7$, $\mu_H = 1.4$, $S_{49} = 0.77$, $\dot{M}_{w,-6} v_{w,8} = 2.5$, $v_{*,6} = 0.85$, and $n_{H,5} = 0.02$, we find that the ionization front is trapped (trapping parameter $\mathcal{T} \sim 1.0$), in agreement with the observations.

Finally, we note that, from ammonia observations in the (1, 1) and (2, 2) transition lines, Churchwell et al. (1990) derived an NH_3 column density toward G13.87+0.28 of $\sim 3 \times 10^{14}$ cm^{-2}. This value is considerably smaller than those derived toward similar compact H II regions, suggesting that the ambient molecular gas toward G13.87+0.28 has a comparatively lower density. Furthermore, observations in the (4, 4) inversion transition of NH_3, by Cesaroni et al. (1992), show the presence of hot gas which has a column density of 2×10^{16} cm^{-2}, about two orders of magnitude higher than that of the cool gas, and which is redshifted by ~ 2 km s^{-1} with respect to the ambient cloud. It is likely that this gas corresponds to the postshock gas in the bow shock.

5. SUMMARY

We mapped, with the VLA, the H92α recombination line and radio continuum emission from three cometary-like H II regions, G13.87+0.28, G32.80+0.19B, and G61.48+0.09B1, and two associated compact H II regions. The main results and conclusions presented in this paper are summarized as follows.

1. The radio continuum image shows that the morphology of G13.87+0.28 exhibits a bright compact head, with a limb-brightened leading edge, and an extended structure of lower brightness trailing opposite to the head. The Lyman continuum photon rate required to explain the observed radio continuum emission can be accounted by an O6.5 ZAMS star. The H92α line maps show a gradient in velocity along the symmetry axis of G13.87+0.28 (P.A. 15°); the velocity decreases from ~ 53 km s^{-1} at the ridge of the head to ~ 47 km s^{-1} in the tail. The observed velocity field and morphology of the ionized gas can be well explained by the bow shock model. We find that the star is moving at an angle of $\sim 60°$ with respect to the line of sight and that the standoff distance of the shock from the star is 0.2 pc. Assuming a momentum rate in the stellar wind of $\dot{M}_* v_* \sim 2.5 \times 10^{-3}\ M_\odot$ yr^{-1} km s^{-1}, appropriate for an O6.5 ZAMS exciting star as suggested by infrared and radio observations, and an ambient hydrogen density of 2×10^3 cm^{-3}, we find that the velocity of the star relative to the ambient cloud is ~ 8.5 km s^{-1}. In addition, we find that the ionization front is trapped ($\mathcal{T} \sim 1$), in agreement with the observations.

2. The radio continuum image of G32.80+0.19B shows that its morphology consists of a moderately bright, arclike head (which does not exhibit limb brightening) and a low-brightness tail that flares away from the axis of symmetry. The H92α line maps show that there is a gradient in the velocity of the ionized gas, running roughly along the symmetry axis of the cometary structure (P.A. $\sim 38°$). The velocity increases smoothly from ~ 14 km s^{-1} at the head's leading edge to ~ 22 km s^{-1} at the tail's edge ($\sim 9''$ behind the head). These characteristics of the ionized gas combined with the similar velocities of the ionized gas at the head position and of the molecular gas toward G32.80+0.19B suggest that this cometary H II region is undergoing a champagne flow.

3. The radio continuum image of G61.48+0.09B1 shows that the brightness distribution is stronger on its eastern side (head) and that it decreases smoothly toward the opposite direction. It does not show sharp leading edges, however. The H92α line maps show a remarkable gradient in the velocity of the ionized gas from this region. The mean velocity increases from ~ 21 km s^{-1} at the leading edge of the head structure to ~ 33 km s^{-1} in the tail's edge, a shift of ~ 12 km s^{-1} over an angular distance of $\sim 15''$. The kinematics observed toward G61.48+0.09B1 is most simply interpreted in terms of bulk outflow motions of the ionized gas away from the molecular gas.

4. The cometary regions G32.80+0.19B and G61.48+0.09B1 are found near (~ 0.4 pc distance) other compact H II regions. Since the closeness of cometary regions to dense, compact H II regions argues against a bow shock hypothesis (Fey et al. 1992), the gregarious nature provides additional support for the champagne hypothesis for the origin of their cometary morphology.

5. We find that the LTE electron temperatures derived from the observations of the H92α line are not reliable estimates of the true electron temperatures. The ratios of true electron temperature to LTE electron temperature range from 1.2 to 2.1, with the higher ratios being found for the H II regions with the largest emission measures.

APPENDIX

CONDITIONS FOR THE STELLAR WIND TO BE CONFINED WITHIN THE CHAMPAGNE FLOW

Franco, Tenorio-Tagle, & Bodenheimer (1990) considered the evolution of an H II region excited by a newly formed massive star born within a molecular cloud that consisted of a small constant-density core of radius R_c surrounded by an envelope with a density profile $\rho \propto r^{-w}$. They found that for clouds with $w \geq 3/2$ (in the limit of $R_c \to 0$), the ionization front is not trapped and the whole cloud becomes ionized and heated to $T \sim 10^4$ K. Under these conditions, in addition to the general expansion of the cloud at $v \sim c_i$

due to the pressure gradient, where c_i is the sound speed of the ionized gas, there is an inner shock that advances into the ionized cloud because the local acceleration of the gas decreases with the radial distance to the star. This shock is mildly supersonic, and the density in the inner region adjusts to the average density given by

$$\rho_{\rm mean}(t) = \left(\frac{3}{3-w}\right)\rho(R_{\rm is}) , \tag{A1}$$

where $R_{\rm is}$ is the position of the shock. Franco et al. (1990) found that for $w < 3$,[3] the radius of this shock increases with time as

$$R_{\rm is}(t) \sim R_c + g(w)c_i t , \tag{A2}$$

where $g(w) = 1 + [3/(3-w)]^{1/2}$. This shock accelerates the gas to velocities of order $g(w)c_i$. This type of evolution corresponds to the so-called champagne phase.

Massive, luminous stars are known to possess high-speed continuous mass loss. It is not known, however, when the star turns on its wind. Here we will assume that the wind appears in a very early stage of the star's evolution, and investigate its role on the dynamical evolution of the H II region. In particular, we want to find out under which conditions the stellar wind remains confined inside the champagne flow. For simplicity, we assume that the star turns on a wind at a time that we set as $t = 0$, when the shock position is $R_{\rm is0}$. The stellar wind will then flow into a fully ionized medium with a density structure determined by the previous champagne flow (eq. [A1]).

Ignoring the free-expansion phase of the stellar wind, we consider only the snowplow phase (Castor, McCray, & Weaver 1975). In this phase, a hot bubble of shocked stellar wind with pressure P_b pushes a shell of swept ambient medium whose mass, $M_{\rm sh}$, grows with time. The position of the swept-up shell, $R_{\rm sh}$, is given by the solution of the energy and momentum equations:

$$\frac{d}{dt}\left(2\pi R_{\rm sh}^3 P_b\right) = \dot{E}_0 - 4\pi R_{\rm sh}^2 P_b \frac{dR_{\rm sh}}{dt} \tag{A3}$$

and

$$\frac{d}{dt}\left(M_{\rm sh}\frac{dR_{\rm sh}}{dt}\right) = 4\pi R_{\rm sh}^2 P_b , \tag{A4}$$

where $\dot{E}_0$ is the mechanical energy of the stellar wind, $\frac{1}{2}\dot{M}_w v_w^2$. The first equation states that the internal energy of the bubble is fed by the energy deposited by the stellar wind and decreases because of the work done to push the shell. The second equation states that momentum of the swept-up shell changes due to the pressure force of the hot shocked wind bubble. Finally, the mass of the swept-up shell expanding inside the champagne flow grows with time as

$$\frac{d}{dt}M_{\rm sh}(t) = 4\pi R_{\rm sh}^2 \rho_{\rm mean}\frac{dR_{\rm sh}}{dt} = 4\pi R_{\rm sh}^2\left(\frac{3}{3-w}\right)\rho_{\rm is0}\left(\frac{R_{\rm is}}{R_{\rm is0}}\right)^{-w}\frac{dR_{\rm sh}}{dt} , \tag{A5}$$

where $\rho_{\rm is0}$ is the density at $R_{\rm is0}$.

We define the variables: $r = R_{\rm sh}/R_{\rm is0}$; $\tau = t/t_0$, where $t_0 = R_{\rm is0}/c_i$; and $m_{\rm sh} = M_{\rm sh}/M_0$, where

$$M_0 = 4\pi R_{\rm is0}^3 \frac{3}{3-w}\rho_{\rm is0} .$$

Equations (A3) and (A4) can be combined, leading, in terms of the new variables, to the equation

$$3\dot{m}_{\rm sh}\dot{r}_{\rm sh}^2 + 3m_{\rm sh}\dot{r}_{\rm sh}\ddot{r}_{\rm sh} + m_{\rm sh}r_{\rm sh}\dddot{r}_{\rm sh} + \ddot{m}_{\rm sh}r_{\rm sh}\dot{r}_{\rm sh} + 2\dot{m}_{\rm sh}r_{\rm sh}\ddot{r}_{\rm sh} = C , \tag{A6}$$

where the derivatives are with respect to τ, and

$$C = \frac{3-w}{6\pi}\frac{\dot{E}_0 t_0^3}{\rho_{\rm is0}R_{\rm is0}^5} . \tag{A7}$$

Equation (A5) becomes

$$\dot{m}_{\rm sh} = \frac{r_{\rm sh}^2\dot{r}_{\rm sh}}{[1+g(\omega)\tau]^w} . \tag{A8}$$

For a density profile of the cloud, $\rho = \rho_{\rm is0}(R_{\rm is}/R_{\rm is0})^{-w}$, and a wind mechanical luminosity, $\dot{E}_0$, equations (A6) and (A8) can be used to solve numerically for the position of the swept-up shell $r_{\rm sh}(t)$, given the initial conditions $r_{\rm sh}(0)$, $\dot{r}_{\rm sh}(0)$, $\ddot{r}_{\rm sh}(0)$, and $m_{\rm sh}(0)$. One such solution is shown in Figure 14, which plots log ($R_{\rm sh}$/pc) versus log (t/yr) for a cloud with a density profile $w = 2$, $R_{\rm is0} = 1 \times 10^{-3}$ pc, and $\rho_{\rm is0} = 10^9 m_{\rm H}$ g cm^{-3}, and a wind luminosity defined by $\dot{M}_w = 1 \times 10^{-6}\ M_\odot$ yr^{-1} and $v_w = 2000$ km s^{-1}. These values are representative of cloud densities and stellar wind strengths expected for high-mass stars. The initial conditions taken to be $r_{\rm sh}(0) = 1 \times 10^{-2}$, $\dot{r}_{\rm sh}(0) = 0$, $\ddot{r}_{\rm sh}(0) = 0$, and $m_{\rm sh}(0) = 1 \times 10^{-4}$. These conditions are arbitrary, but the solution for $R_{\rm sh}$ does not change for $t > t_0$, as discussed below. The broken line corresponds to the shock radius of the champagne flow, and the solid line

[3] We will not discuss density gradients with $w > 3$ which produce strong accelerating shocks (see discussion in Franco et al. 1990) because our simple assumptions will probably break down.

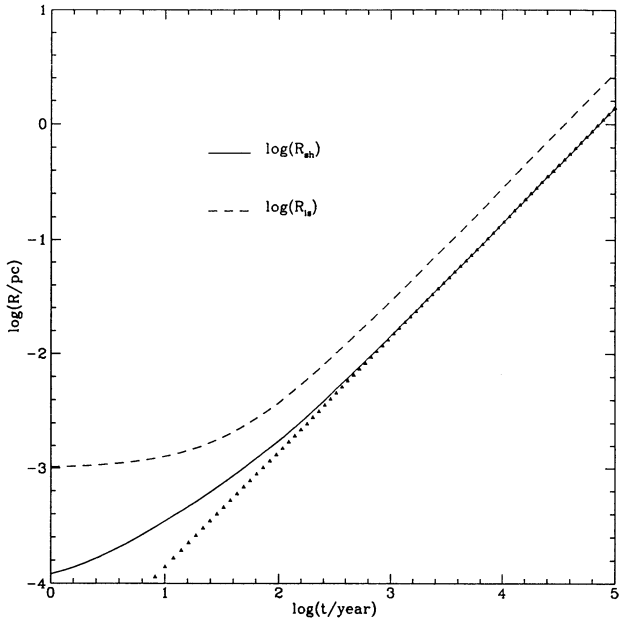

FIG. 14.—Shown as a function of time are the radius of the swept-up shell of the stellar wind, R_{sh} (*solid line*); the shock radius of the champagne flow, R_{is} (*dashed line*); and the power-law solution for R_{sh} (*points*).

corresponds to the radius of the shell swept up by the stellar wind. One can see that in this case the stellar wind is always confined within the champagne flow.

Fortunately, there is no need to study the parameter space, since, with a very simple approximation, equation (A6) allows for a power-law solution valid for $t > t_0$. Using the approximation $r_{is} = g(w)\tau$ in equation (A8), i.e., ignoring the initial shock radius of the champagne flow, we find a power-law solution for R_{sh} of the form

$$R_{sh}(t) = R_0\left(\frac{t}{t_0}\right)^{\alpha}, \tag{A9}$$

such that

$$\alpha = \frac{w+3}{5} \tag{A10}$$

and

$$R_0 = \left[\frac{3-w}{6\pi}\frac{\dot{E}_0 t_0^3}{\rho_{is0}}\frac{g(w)^w}{F(w)}\right]^{1/5}, \tag{A11}$$

where

$$F(w) = \frac{(77 + 3w - 2w^2)(3+w)^2}{125(9-2w)}.$$

This power-law solution, shown by the points in Figure 14, matches the numerical solution for $t > t_0$. This solution shows that, for a density gradient with $w < 2$, the swept-up shell decelerates slightly with time; for $w = 2$ it has a constant velocity, and for $w > 2$ it accelerates slightly with time. We note that for $w = 0$ (i.e., a constant-density medium) we recover the expression for the radius of the shell as a function of time given by Castor et al. (1975; their eq. [6]). Note, however, that the discussion presented here applies only for $3/2 \leq w < 3$.

Using the power-law solution, we find that the stellar wind is confined within the champagne flow if the condition

$$\frac{1}{R_{is0}}\left[\frac{3-w}{6\pi}\frac{\dot{E}_0 t_0^3}{\rho_{is0}}\frac{g(w)^w}{F(w)}\right]^{1/5}\left(\frac{t}{t_0}\right)^{\alpha} < 1 + g(w)\left(\frac{t}{t_0}\right)$$

is fulfilled. In particular, for typical wind parameters, ambient medium densities $n \geq 10^6$ cm^{-3} at 0.01 pc are required to confine the stellar wind. Molecular densities in the range 10^6–10^7 cm^{-3} are typical of warm molecular cores associated with recently formed young stars. Therefore, for high enough cloud densities, the stellar wind will remain well inside R_{is} and the dynamics of the ionized gas will be dominated by the champagne flow.

We thank the referee, M.-M. Mac Low, for useful comments on the paper. G. G. acknowledges the warm hospitality and support from the Instituto de Astronomía, UNAM. This research has been partially supported by the Chilean FONDECYT under grant 0907/92 and by the Mexican grants CONACYT 0752-E and DGAPA IN100291.

REFERENCES

Bodenheimer, P., Tenorio-Tagle, G., & Yorke, H. W. 1979, ApJ, 233, 85
Brocklehurst, M. 1970, MNRAS, 148, 417
Brocklehurst, M., & Leeman, S. 1971, Astrophys. Lett., 9, 35
Brocklehurst, M., & Seaton, M. J. 1972, MNRAS, 157, 179
Brown, R. L., Lockman, F. J., & Knapp, G. R. 1978, ARA&A, 16, 445
Castor, J., McCray, R., & Weaver, R. 1975, ApJ, 200, L107
Cesaroni, R., Walmsley, C. M., & Churchwell, E. 1992, A&A, 256, 618
Chini, R., Krügel, E., & Wargau, W. 1987, A&A, 181, 378
Churchwell, E., Walmsley, C. M., & Cesaroni, R. 1990, A&AS, 83, 119
Deharveng, L., & Maucherat, M. 1978, A&A, 70, 19
Felli, M., & Harten, R. H. 1981, A&A, 100, 42
Fey, A. L., Claussen, M. J., Gaume, R. A., Nedoluha, G. E., & Johnston, K. J. 1992, AJ, 103, 234
Franco, J., Tenorio-Tagle, G., & Bodenheimer, P. 1990, ApJ, 349, 126
Garay, G. 1990, in Radio Recombination Lines: 25 Years of Investigation, ed. M. A. Gordon & R. L. Sorochenko (Dordrecht: Kluwer), 73
Garay, G., & Rodríguez, L. F. 1983, ApJ, 266, 263
Garay, G., Rodríguez, L. F., Moran, J. M., & Churchwell, E. 1993, ApJ, 418, 368
Garay, G., Rodríguez, L. F., & van Gorkom, J. H. 1986, ApJ, 309, 553
Goldberg, L. 1968, in Interstellar Hydrogen, ed. Y. Terzian (New York: Benjamin), 373
Hartigan, P., Raymond, J., & Hartmann, L. 1987, ApJ, 316, 323
Kurtz, S., Churchwell, E., & Wood, D. O. S. 1994, ApJS, 91, 659
Macdonald, G. H., Little, L. T., Brown, A. T., Riley, P. W., Matheson, D. N., & Felli, M. 1981, MNRAS, 195, 387
Mac Low, M.-M., Van Buren, D., Wood, D. O. S., & Churchwell, E. 1991, ApJ, 369, 395
Reid, M. J., & Ho, P. T. P. 1985, ApJ, 288, L17
Shaver, P. A. 1980, A&A, 91, 279
Tenorio-Tagle, G. 1979, A&A, 71, 59
Van Buren, D. 1985, ApJ, 294, 567
Van Buren, D., & Mac Low, M.-M. 1992, ApJ, 394, 534
Van Buren, D., Mac Low, M.-M., Wood, D. O. S., & Churchwell, E. 1990, ApJ, 353, 570
van Gorkom, J. H., Goss, W. M., Shaver, P. A., Schwarz, U. J., & Harten, R. H. 1980, A&A, 89, 150
White, G. J., & Fridlund, C. V. M. 1992, A&A, 266, 452
Wink, J. E., Altenhoff, W. J., & Mezger, P. G. 1982, A&A, 108, 227
Wood, D. O. S., & Churchwell, E. 1989, ApJS, 69, 831
Yorke, H. W., Tenorio-Tagle, G., & Bodenheimer, P. 1983, A&A, 127, 313
———. 1984, A&A, 138, 325